Article

# Raman Spectroscopy and Imaging of Ultralong Carbon Nanotubes

Stephen K. Doorn, Lianxi Zheng, Michael J. O'Connell, Yuntian Zhu, Shaoming Huang, and Jie Liu

## More About This Article

Additional resources and features associated with this article are available within the HTML version:

- Supporting Information
- Links to the 8 articles that cite this article, as of the time of this article download
- Access to high resolution figures
- Links to articles and content related to this article
- Copyright permission to reproduce figures and/or text from this article

View the Full Text HTML

# Raman Spectroscopy and Imaging of Ultralong Carbon Nanotubes

**Stephen K. Doorn,\*,[†] Lianxi Zheng,[†] Michael J. O'Connell,[†] Yuntian Zhu,[†] Shaoming Huang,[‡] and Jie Liu[‡]**

*Los Alamos National Laboratory, Los Alamos, New Mexico 87545 and Department of Chemistry, Duke University, Durham, North Carolina 27708*

Raman spectroscopy and confocal Raman imaging with 514 nm excitation was performed on recently developed ultralong carbon nanotubes grown by the "fast-heating" chemical vapor deposition (CVD) method. The ultralong nanotubes are found to consist of both semiconducting and metallic types, with spectra that are consistent with the nanotubes being single walled. Characterization of nanotube diameters shows that short nanotubes appearing near the sample catalyst region have a broader distribution than is observed for the ultralong nanotubes. The narrow diameter distribution is determined by uniformity of catalyst particle size and gives additional evidence for the proposed "kite" mechanism for long nanotube growth. Raman imaging was performed over large length scales (up to 140 $\mu$m). Imaging reveals the ultralong nanotubes to be of high quality, with a very low defect density. Variations in G-band frequencies and intensity demonstrate the occurrence of minor structural changes and variations in nanotube−substrate interaction along the length of the nanotubes. Evidence also demonstrates that larger structural changes resulting in a full chirality change can occur in these nanotube types to produce a metal-to-semiconductor intramolecular junction.

## Introduction

Recent advances in CVD growth methods for synthesis of carbon nanotubes have resulted in production of the longest individual nanotubes reported to date.[1−4] The "fast-heating" method required for producing this new class of nanotubes has resulted in lengths from 1.5 to 4 cm being reported.[3,4] Nanotubes of such macroscopic lengths hold significant potential and inherent advantages over shorter materials for future applications in nanoelectronics, sensors, and high-strength, lightweight materials. The increased interaction lengths available in ropes and composites of these individual nanotubes will result in greater materials strengths. The ability to specifically locate and orient nanotubes through this growth method can result in addressable arrays important for large-scale device and sensor applications.[2] Additionally, their macroscopic lengths raise the intriguing potential that they may be capable of displaying stable electronic and physical properties over large length scales. Thus, the potential for using these ultralong nanotubes in novel ways not possible with shorter tubes will rely on large-scale uniformity in their structural and electronic behavior. Evaluation of the uniformity of their properties over macroscopic lengths is therefore important yet remains to be determined.

Closely tied to a better understanding of the evolution of structural/electronic characteristics over large length scales in ultralong nanotubes is the importance of controlling their growth processes. A greater understanding of their growth and termination mechanisms is therefore required. Recent evidence supports a tip growth mechanism for the ultralong nanotubes,[3] but additional results are required to further describe the important parameters in the process and confirm the tip growth hypothesis. During synthesis, in addition to the ultralong nanotubes, a significant number of shorter nanotubes (<100 $\mu$m) are also produced at the catalyst deposition site. Determination of the relative diameter distributions of the two species of nanotubes may help address why only a subset of nanotubes is able to grow to macroscopic lengths.

Raman spectroscopy provides an excellent tool for probing this new class of nanotubes to address a number of the issues raised above. Single-nanotube Raman spectroscopy has been demonstrated to be a powerful technique for electronic and structural characterization of individual nanotubes less than 1 $\mu$m in length[5,6] and also for small nanotube bundles.[7] Single-nanotube sensitivity is possible due to the large density of states accessed with resonance excitation, allowing high-quality spectra to be obtained with no additional enhancement mechanisms being required. Recently, near-field Raman techniques have been demonstrated to reveal unprecedented detail in the vibrational structure of single nanotubes.[8,9] Confocal Raman imaging of relatively short nanotubes over lengths of ∼2−10 $\mu$m has also been demonstrated as a successful means for mapping of nanotube vibrational/structural details[10−12] and should prove to be a fruitful technique complementary to near-field optical and scanning probe methods (such as STM) for evaluating these new nanotube structures over large length scales.

Confocal Raman imaging provides spatially resolved distributions of nanotube vibrational and, therefore, structural behavior. Through the resonance Raman effect this approach will also yield information on variations in electronic behavior due to the presence of structural defects or through variable interactions with the substrate. In addition to mapping of minor structural variations and defects, the technique also has the potential to reveal a complete change in nanotube chiral structure. Such measurements on ultralong nanotubes will be invaluable for evaluating the structural uniformity of these systems that in turn will determine their transport and materials characteristics.

In this paper we present results for Raman imaging on ultralong (300 $\mu$m to 3 mm in length) nanotubes produced by

---

\* To whom correspondence should be addressed. E-mail: skdoorn@lanl.gov.
† Los Alamos National Laboratory.
‡ Department of Chemistry, Duke University.

the "fast-heating" CVD method.[1] The diameter distribution of the ultralong nanotubes present in our sample was characterized and compared to that of shorter nanotubes found on the same substrate with results being consistent with the proposed "kite" mechanism for tip growth.[3] Nanotubes were characterized by taking spectra periodically over lengths up to 1 mm and via Raman imaging performed over large length scales (40 to 140 $\mu$m). In general, these nanotubes were found to be of high structural quality, while minor local variations in vibrational and electronic structure were observed. Evidence is also found for the occurrence of larger structural changes, resulting in a chiral shift along the length of one observed nanotube.

## Experimental Section

The carbon nanotubes were grown by catalytic chemical vapor deposition using the fast-heating method,[1-3] with methane ($CH_4$) as the carbon source and Fe/Mo as the catalyst. Before growth, Fe/Mo carbonyl complex (from $Fe(CO)_5$/$Mo(CO)_6$ solution)[13] was applied on a silicon (with 600 nm $SiO_2$) wafer. The Si wafer carrying the catalyst was introduced into a quartz tube and heated at 650 °C for 5 min in a hydrogen atmosphere in order to decompose and reduce the catalyst complex into Fe/Mo nanoparticles. The Si wafer was then moved away from the tube center, and the methane hydrogen mixture (850 sccm $CH_4$ and 400 sccm $H_2$) was introduced into the reactor while heating the tube to 900 °C. Once the reactor reached the desired temperature, the Si wafer was quickly transferred into the center area of the tube. The growth lasted for 30 min and was stopped by switching the gas mixture to argon and cooling the furnace to room temperature.

Scanning electron microscopy (SEM) was performed on a JEOL 6300FXV field emission instrument with a 1 kV acceleration voltage and 15 mm working distance. Atomic force microscopy (AFM) imaging was performed in tapping mode using a Digital Instruments Multi-Mode SPM Nanoscope IIIa.

Raman imaging and spectroscopy at 514 nm excitation was performed through a confocal imaging Raman microscope (Kaiser Optical). Image spectra were obtained at 0.5−1.0 $\mu$m spacings over the area of the images. Excitation was performed with 6 mW of light focused through a 100X, 0.9 N.A. microscope objective, providing a 1 $\mu$m spot size. The excitation spot size was confirmed by taking a line profile across a single nanotube, perpendicular to its length. Raman scattered light was collected through a fiber optic and dispersed onto a CCD camera for detection. Typically, spectra were collected as averages of two 4 s integrations. Raman images are generated from the integrated intensity over the nanotube G-band spectral region (1500−1650 $cm^{-1}$).

## Results and Discussion

**General Features.** As seen in an SEM image (Figure 1) of the nanotube sample used for these investigations, two zones of nanotube growth behavior occur. The first of these zones consists of relatively dense growth of short entangled nanotubes that occurs near the catalyst material (left edge of Figure 1). The second zone encompasses the area over which much longer (up to 3 mm for the longest) nanotubes are observed to grow perpendicular to the catalyst stripe. The longer nanotubes are also found to be well separated from each other, with typical spacings of 10 $\mu$m or more. AFM imaging and height profiling of these ultralong nanotubes is consistent with all nanotubes greater than 300 $\mu$m in length existing as single isolated nanotubes and not as small bundles or closely spaced but isolated
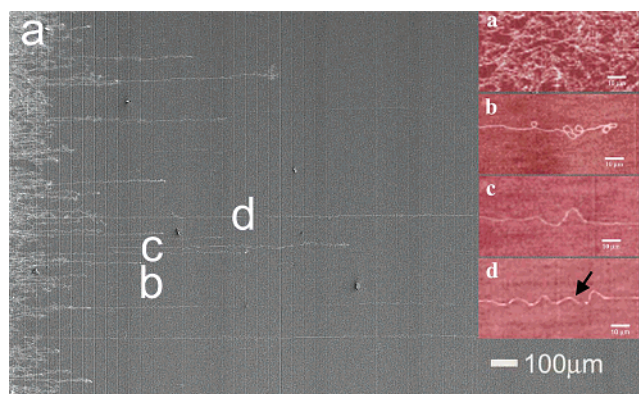


**Figure 1.** High-resolution SEM image of the ultralong nanotube sample used for Raman imaging investigations. Highlighted locations correspond to the regions covered by Raman imaging in (a) Figure 2a, (b) Figure 2d, (c) Figure 4, and (d) Figure 6. (Note that Raman image orientation is horizontally reversed in comparison to the SEM images.)

nanotubes lying within the 1 $\mu$m spatial resolution of the Raman microscope (see Supporting Information). Also seen in the SEM image are a number of silicon surface defects and specks that serve as landmarks for finding different nanotube features. Observation of these landmarks in the microscope bright-field imaging mode allowed reproducible return to specific nanotube locations for Raman and AFM imaging.

Shown in Figure 2a is a typical Raman image and representative spectra (Figure 2b,c) obtained near the catalyst material (see Figure 1, highlighted region a). As seen in the image, many closely spaced nanotubes are present in this region. Their spectra display the usual features for nanotubes, including radial breathing modes (RBMs) at low frequency and the G-peak features near 1600 $cm^{-1}$. Notably, multiple radial breathing modes are present in most spectra obtained in this region, consistent with the relatively dense overlap of individual short nanotubes found in Figure 1. Due to the 1 $\mu$m laser spot size used for obtaining the Raman images, individual nanotubes must be well separated to be resolved from each other. Single-nanotube resolution of the short nanotubes grown in the catalyst region is not possible due to the high density of growth. However, single-nanotube resolution of the ultralong nanotubes is obtainable due to the large spatial separations (typically >10 $\mu$m) between the long nanotubes found in our sample.

Shown in Figure 2d is a representative Raman image and spectra (Figure 2e,f) for the ultralong nanotube highlighted as region b in Figure 1. This image demonstrates well the ability of Raman imaging to map out large-scale features of the nanotube, such as swirls or oscillations, that can be directly mapped to features observed in the SEM image (Figure 1b). As demonstrated by the nanotube in Figure 2d, the G-peak Raman band is typically easily observed for the ultralong nanotubes. However, the nanotube in Figure 2d does not display a radial breathing mode. This is true of the majority of the ultralong nanotubes that were observed, indicating a lack of strong resonance between the laser excitation energy and the singularities in the density of states for these particular nanotube chiralities. Enhancement of the G peak in this case results from resonance of the Raman scattered photon with a lower lying electronic transition.[14,15] In this case of electronic resonance with the scattered photon energy, the RBM scattered photon energy is not expected to be shifted sufficiently (due to its much lower vibrational frequency) to overlap the transitions resonant with the G-peak scattered photon. Thus, it is possible for the G peak to be enhanced while the RBM is not.
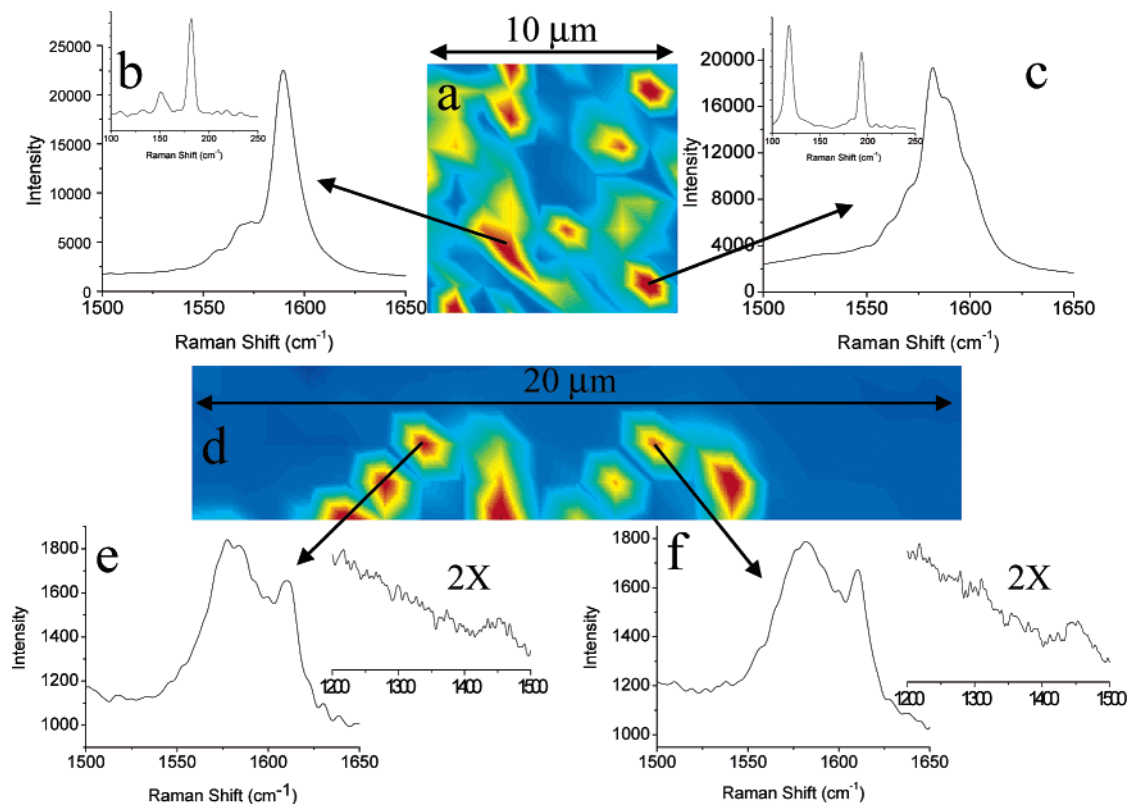
Imaging of Ultralong Carbon Nanotubes

*J. Phys. Chem. B, Vol. 109, No. 9, 2005* **3753**



**Figure 2.** (a) Raman spectral image and (b,c) representative G-band and RBM (inset) spectra obtained from short nanotubes located within the catalyst deposition area (highlighted region a in Figure 1). (d) Raman image and (e,f) representative G- and D-band (inset) spectra obtained from a single ultralong nanotube (highlighted region b in Figure 1). Note that the D-band intensities have been magnified by a factor of 2 relative to the G-band scale. The weak band at 1450 cm$^{-1}$ in the D-band spectra is a substrate peak.

We also note that the commonly observed D band (typically found near 1350 cm$^{-1}$) is either very weak or not observed at all for both the ultralong nanotube and catalyst regions in our sample. This observation indicates that the nanotubes grown via the fast heating CVD method are of high structural quality with a relatively low concentration of defect sites. As seen in Figures 2 and 4−6 (see also Supporting Information), for the majority of nanotubes probed the D band is below the S/N level of the spectra. If the peak-to-peak noise level is taken as a conservative limit for D-band intensity for the spectra in which this feature is not clearly observed, G/D ratios in our samples are found to range from a minimum of 60 to as high as 500. This can be compared to typical G/D ratios of ∼30 for HiPco nanotubes and 190 for the highest quality laser oven nanotubes.[16] Only one of the sampled nanotubes displays a clear D-band (Figure 5b) with a G/D ratio of 20. Although a general lack of defect bands is observed, localized defects may still occur, as demonstrated in Figure 5a(*ii*).

Recently produced shorter CVD nanotubes using similar growth methods[17] have resulted in the production of double-walled nanotubes, suggesting that nanotubes observed in our sample may be double walled as well. However, Raman spectra observed in the ultralong growth region in the current study are consistent with the observed nanotubes being single walled. Double-walled nanotubes typically display complex, multi-peaked G-band spectra.[18,19] Typically observed G-peak spectra (see Figures 2f, 4, and 5 and Supporting Information) for the ultralong nanotubes display a relatively clean two-peak (G$_+$ and G$_-$) structure similar to that observed for isolated short single-walled nanotubes.[5,6] Although a single-walled characterization of the ultralong nanotubes is indicated, the G-peak analysis is not definitive. Recent demonstration of infrared light emission from these ultralong nanotubes,[20] however, provides additional

evidence that they are single walled. Ultimately, resolution of this point will require TEM imaging of the quick-heat samples. We are currently developing modified substrates for growth that will allow these TEM measurements to be made.

**Diameter Distribution.** Large area imaging of nanotubes at several locations along the catalyst stripe on our sample substrate allowed characterization of the general nanotube diameter distribution produced. This distribution is shown in Figure 3a and results from a sampling of the RBM frequency for 170 individual nanotubes (with $\nu_{RBM}$ = 248 cm$^{-1}$ nm/$d_t$, appropriate for CVD grown nanotubes on a silicon substrate).[6] The majority of observed nanotubes are found to be of large diameter, with a peak in the distribution at 1.7 nm. The distribution is quite broad, however, with a significant number of smaller diameter nanotubes being produced and a total span ranging from 0.8 to 2.4 nm.

Measurements on nanotubes with lengths greater than 300 μm produce a significantly different diameter distribution, as seen in Figure 3b. As RBMs were observed for only four of these ultralong nanotubes, the frequency difference ($\Delta\nu_G$) between the G$_+$ and G$_-$ peaks was used to estimate the diameter ($d_t$)[6]

$$\Delta\nu_G = C/d_t^2 \qquad (1)$$

where $C$ = 47.7 cm$^{-1}$ nm$^2$ for semiconducting nanotubes and 79.5 cm$^{-1}$ nm$^2$ for metallics. Comparison of the calculated diameters using eq 1 to results obtained from the RBM for the few nanotubes for which both modes are observed shows that use of the G-peak frequencies for diameter approximation can result in an error of ca. ±0.2 nm. The diameter distribution obtained from this method is still found to peak near 1.7 nm but is significantly narrower than that found for the shorter tubes
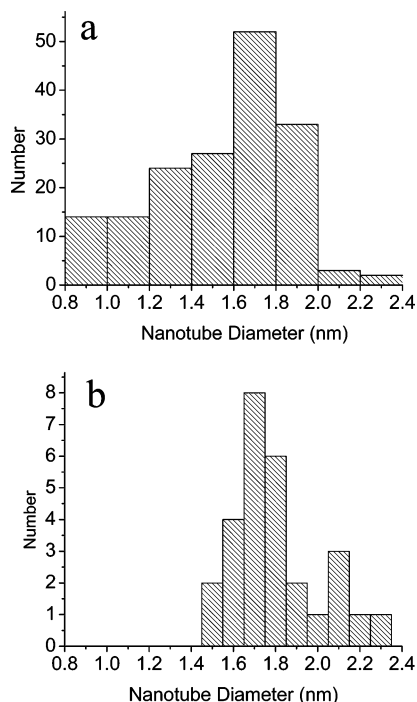
**Figure 3.** (a) Diameter distribution of 170 individual nanotubes sampled within the catalyst deposition region. Diameters ($d_t$) were determined from observed RBMs using the relation $\nu_{RBM} = 248$ cm$^{-1}$ nm/$d_t$. (b) Diameter distribution of 28 different ultralong nanotubes. Approximate diameters were determined using eq 1.

observed in the catalyst region. The ultralong nanotubes are found to consist of only large diameters, with the narrowest observed nanotubes being 1.4 nm.

The differences in diameter distribution between short nanotubes found in the catalyst region and the ultralong nanotubes, particularly the absence of small diameters and narrower distribution overall in the ultralong nanotubes, suggest very different growth mechanisms for production of short vs long nanotubes in the fast-heating process. A tip growth mechanism has been proposed for the ultralong nanotube growth process[1] and is supported by recent results.[3] Briefly, the large temperature difference between substrate and flow gas in the fast-heating process results in convective forces that lift the growing nanotube off the substrate surface at the nucleation stage, followed by tip growth along the direction of the gas flow. The broader diameter distribution for short nanotubes suggests that the growth mechanism for a significant fraction of the nanotubes found in the catalyst region may, instead, be basal growth, as found in conventional CVD processes.[21] It is possible that for catalyst particles that stay on the substrate their size can change due to aggregation or formation of an alloy with the substrate. Catalysts suspended on the tip of a growing nanotube, however, have their size fixed. Since the catalysts we use are relatively uniform with narrow diameter distributions[13] and the "lift up" process happens during the first few seconds of growth, these particles have little opportunity to change their morphology. A narrow diameter distribution for all long nanotubes is expected to result. Short nanotubes can nucleate at later times during growth, after catalyst aggregation and/or evaporation of metal atoms has occurred, resulting in a broader diameter distribution. Thus, the observed differences in diameter distribution add additional support to the proposed growth mechanism for ultralong nanotubes: nanotube lift up during nucleation and initial growth followed by extended tip growth.

**Imaging Over Large Length Scales.** Confocal Raman imaging of several of the ultralong nanotubes was performed over large length scales (40 $\mu$m or more). Typical nanotube images taken in the ultralong growth region (regions b and c, Figure 1) are shown in Figures 2d and 4a, respectively. By comparing the Raman images to the SEM images (Figure 1) obtained over the same region, it is seen that the Raman imaging accurately reproduces the major physical features, such as swirls or long straight segments, found in the SEM. The relative ease with which the 140 $\mu$m long image shown in Figure 4a was obtained demonstrates that confocal Raman imaging can be a powerful tool for mapping out vibrational features over large length scales. Mapping of vibrational variations over such scales allows an evaluation of structural uniformity, potential characterization and location of defect sites, and a probe of localized environmental interactions.

The nanotubes imaged in Figures 2 and 4 display the typical two-peak G-band (tangential mode) structure found near 1600 cm$^{-1}$. The higher frequency (G$_+$) peak corresponds to carbon–carbon deformations along the tube axis, while the low-frequency (G$_-$) peak corresponds to deformations perpendicular to the axis.[22,23] The Breit–Wigner–Fano line shape of the G$_-$ peaks shown for the nanotube in Figure 2d–f indicates this to be a metallic nanotube.[23–25] The peak separation of 28 cm$^{-1}$ gives it an approximate diameter of 1.7 nm (using eq 1). The narrow Lorentzian line shape observed for the G-peak features for the nanotube shown in Figure 4a–f identifies it as being semiconducting in nature.[23,25] The average G-peak separation of 23 cm$^{-1}$ for this nanotube gives it an approximate diameter of 1.4 nm.

The G-peak frequencies are found to be quite stable (within 1 cm$^{-1}$) over the imaged length of the nanotube shown in Figure 2d, indicating that a high degree of structural stability is present for this segment. However, significant changes in both G$_+$- and G$_-$-peak frequencies are found over the length of the semiconducting segment imaged in Figure 4. G$_+$ frequencies range from 1590 to 1586 cm$^{-1}$, while the G$_-$ band is found to shift from 1576 to 1565 cm$^{-1}$. These frequency shifts can result from both nanotube structural changes or through environmental interactions.

Environmentally induced changes in G-peak frequencies have been observed to originate from withdrawal or donation of electron density to the nanotube, either through internal doping,[26] or through external chemical interactions,[27–29] and also can occur through strain interactions.[30] Withdrawal of electron density results in a frequency increase. A tangential mode shift of 250 $\pm$ 80 cm$^{-1}$ per electron per carbon atom has been suggested through electrochemical tuning of the nanotubes,[28] while bisulfate oxidation has been estimated to produce a shift of 320 cm$^{-1}$ per hole per carbon atom.[27] Our observed frequency shifts of up to 4 cm$^{-1}$ in the tangential mode could thus result from interactions with the silicon substrate that could generate a small degree of shift in electron density to or from the substrate.

The observed frequency shifts could also arise from minor structural changes or even large-scale changes in nanotube chirality. We observe a change in the G-peak separation from a maximum of 25 cm$^{-1}$ to a minimum of 21 cm$^{-1}$, which (using eq 1) may indicate a possible diameter change from 1.4 to 1.5 nm (although such a small change is well within the expected approximation error of eq 1). A true 0.1 nm diameter change would also require a shift in chirality. If such a change were accompanied by a large change in chiral angle, we would expect to see significant changes in relative intensity between the two
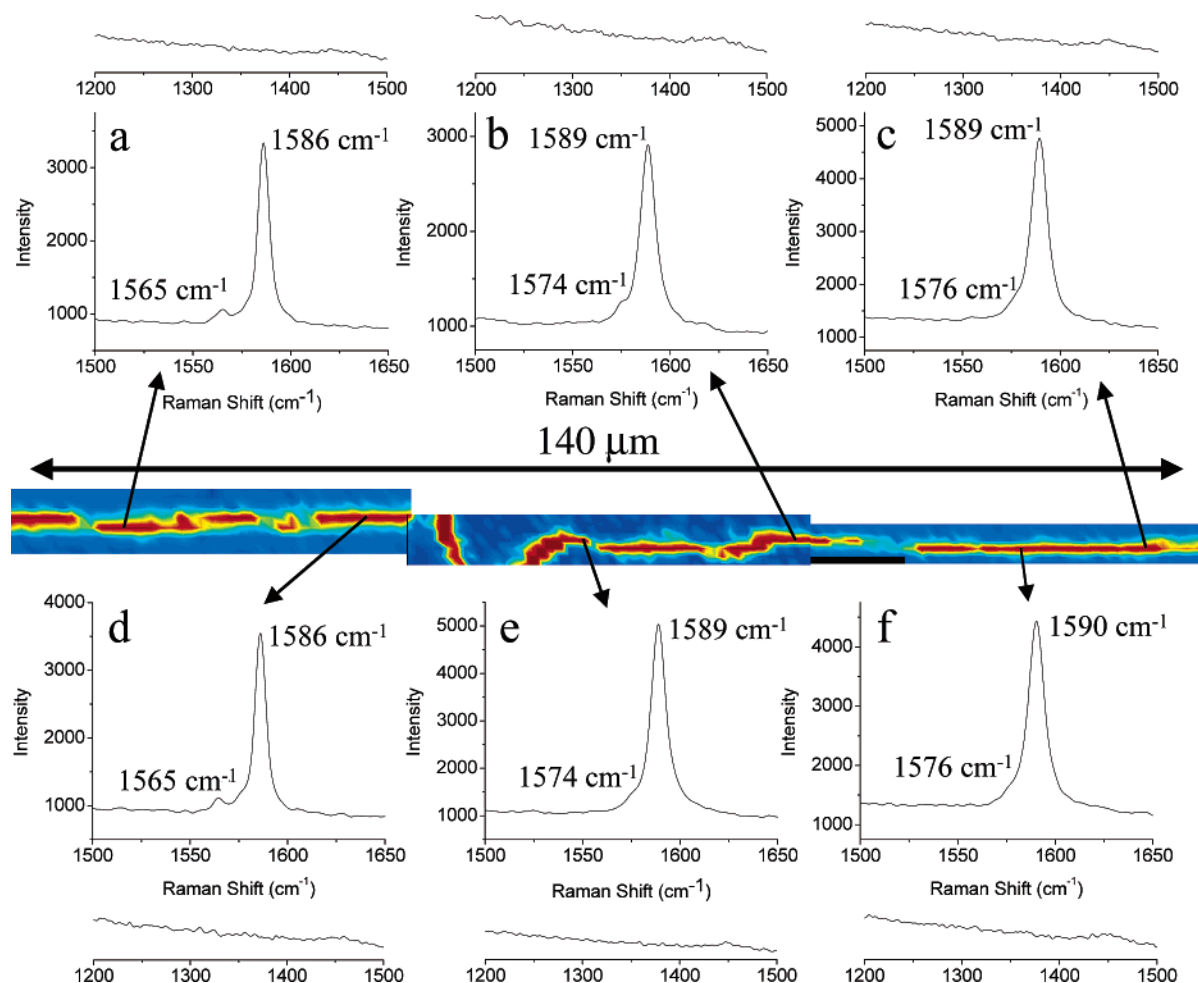
Imaging of Ultralong Carbon Nanotubes

*J. Phys. Chem. B, Vol. 109, No. 9, 2005* **3755**



**Figure 4.** Raman spectral image and (a–f) representative D- and G-band spectra obtained from the ultralong nanotube highlighted in region c of Figure 1. Note the D-band spectral intensity scale is the same as that for the G-band spectra. The weak band at 1450 cm$^{-1}$ is a substrate peak.

G-band subpeaks.[7] Relative intensities (Figure 4 a–f), however, remain stable across the imaged segment. Additionally, the G-peak frequency difference is not a simple transition from high to low but instead varies from 21 to 25 to 23 cm$^{-1}$ across the imaged segment. Thus, the observed G-band behavior is most likely a result of a combination of minor, localized, structural changes and frequency perturbation through environmental interactions rather than a complete chirality shift.

In addition to minor G-band frequency shifts we observe reproducible intensity changes along the nanotube segment shown in Figure 4. These intensity fluctuations are likely caused by localized variations in the nanotube energy levels, causing relative changes in the degree of resonance obtained with the Raman excitation or scattered wavelengths.[11] Such electronic energy perturbations can result from the occurrence of localized defect sites or, as discussed above, environmental interactions. The observation that the ultralong nanotubes have no detectable D band suggests that defect sites will not play a major role in alteration of energy levels. Instead, these intensity changes mark the location of variations in interaction between the nanotube and the silicon substrate.

The results shown in Figure 4 demonstrate that minor, relatively localized, changes in molecular structure and electronic behavior can occur in the ultralong nanotube samples on length scales of tens of micrometers. Such structural instabilities can act as scattering sites impacting transport and optical properties. On even longer length scales, however, we find that stable G-band spectra can occur. Figure 5 shows spectra for two additional nanotubes obtained over a total length of 1 mm.

G-Band frequencies are stable within ±1 cm$^{-1}$. Thus, we observe for the majority of nanotubes that large-scale structure and chirality remains uniform for extended lengths while more localized structural and electronic instabilities can occur.

**Nanotube Chirality Shift.** Large structural changes that produce a full chiral shift, or intramolecular junction (IMJ), may result in single nanotubes that act as diodes, rectifiers, and electrooptical elements and may eventually be capable of replacing complex source-drain structures in nanotube FETs.[31–33] A number of theoretical studies have probed IMJ electronic[34–38] and optical properties,[39] while recent STM imaging and density of states measurements have provided direct evidence for their occurrence.[40,41] Optical spectroscopic probes, including Raman imaging, may provide a faster and more accessible means for detection and structural characterization of nanotube IMJs.

We find direct Raman evidence for the occurrence of an IMJ in the longest nanotube shown in Figure 1. A Raman image of region d of Figure 1 is shown in Figure 6. G-Band spectra across the length of this region (Figure 6a–e) show an initial Lorentzian line shape (Figure 6a) that goes through a transition region (Figure 6b–d) and ends in a Breit–Wigner–Fano line shape (Figure 6e). We find that the Lorentzian line shape remains stable along the length of the nanotube up to its initiation point in the catalyst region, while the Breit–Wigner–Fano line shape remains stable to the nanotube tip. The shift from Lorentzian to Breit–Wigner–Fano line shape indicates the nanotube undergoes a semiconductor-to-metallic transition.

Our ability to image the transition region over which this chiral shift in electronic properties occurs allows an evaluation
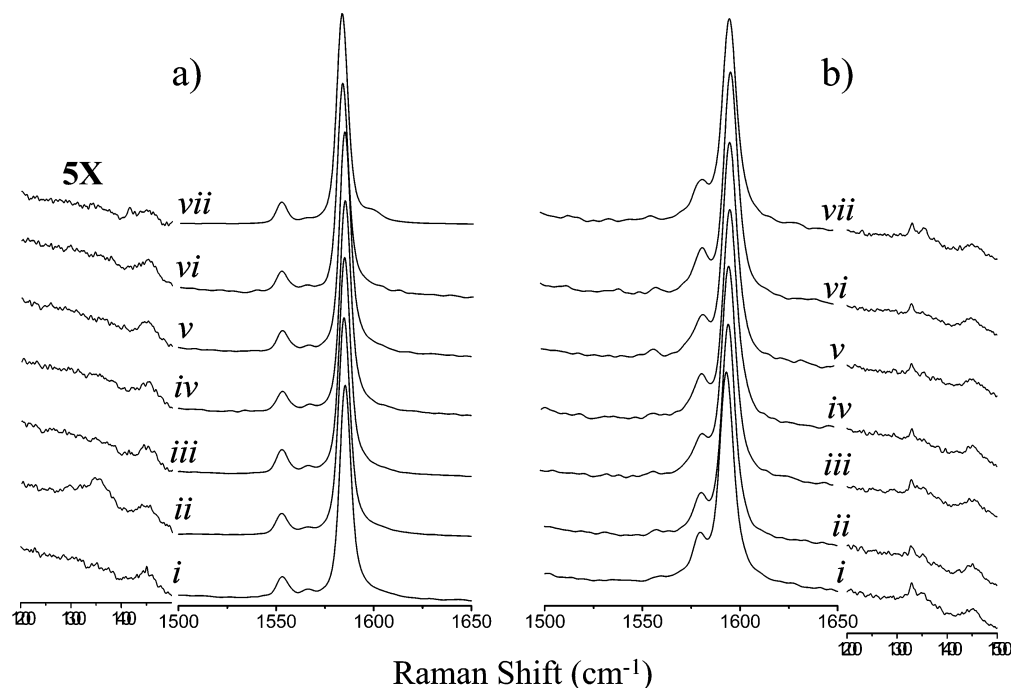
**Figure 5.** Raman point spectra taken along the length of two additional ultralong nanotubes showing D- (1200−1500 cm$^{-1}$) and G-band (1500−1650 cm$^{-1}$) regions. (a) Point spectra were taken at relative distances (in microns) along the nanotube of (*i*) 0, (*ii*) 100, (*iii*) 200, (*iv*) 300, (*v*) 700, (*vi*) 900, and (*vii*) 950. The D-band intensity scale has been magnified by 5× relative to that of the G-band spectra. (b) Point spectra taken at relative distances (in micrometers) of (*i*) 0, (*ii*) 150, (*iii*) 850, (*iv*) 900, (*v*) 950, (*vi*) 1050, and (*vii*) 1150. The D-band intensity scale is the same as that for G-band spectra. Note the weak band at 1450 cm$^{-1}$ is a substrate peak.

of the structural transformation required to form the IMJ. The broad, weakly structured G-peak spectra observed at the IMJ transition region (Figure 6b−d) indicate a lowering of nanotube symmetry during the transition. Geometric modeling of nanotube structure[40,41] has demonstrated that the M−S transition can occur through incorporation of multiple pentagon−heptagon (or 5−7) defect pairs in the transition region. The presence of these defects will result in a decreased nanotube symmetry consistent with our observations. As found for the other nanotubes in this sample, the defect band is unobservable across the IMJ transition region. The weakness in the D band indicates that the 5−7 defects occur only over a very narrow distance−within the spatial resolution of our imaging. Additionally, we observe a RBM at 147 cm$^{-1}$ for the metallic side of this nanotube, indicating a diameter of 1.69 nm (see Figure 7). The RBM becomes very weak on passing through the IMJ transition but is still observed at nearly the same frequency, indicating that the IMJ transition occurs with very little diameter change. The observed decrease in RBM intensity on transitioning from the metallic to semiconductor region is expected. For nanotubes of identical diameter but different electronic nature (metallic vs semiconductor), electronic resonances will be very different. Thus, if the excitation wavelength is within the resonance window for the metallic nanotube (resulting in enhancement of its RBM), resonance enhancement of the semiconducting RBM is expected to be much weaker. Note also that the integrated intensity over the G-band region is stronger for the metallic nanotube than that observed for the semiconductor (see Figure 6).

Given the 1 $\mu$m spatial resolution of the Raman imaging it is reasonable to question whether the region imaged in Figure 6 is due to a single nanotube with an IMJ transition or is it two different nanotubes resting side-by-side. If the data are from two nanotubes, the spectra in the overlapping region would be expected simply to be the sum of the G-peak spectra from the different nanotube types. This, however, is not the case (see

Supporting Information). Additionally, AFM imaging of the transition region is consistent with only one nanotube existing in the imaged region (see Supporting Information). AFM height profiles across three separate cross-sections of the junction region are consistent with a single nanotube of approximately 1.7 nm diameter. Admittedly, AFM lateral resolution is not sufficient to discriminate between two nanotubes lying side-by-side, but no separate nanotubes are found to branch into or out of this region within the 240 $\mu$m imaged via AFM. Finally, the image spectra of Figure 6 were also obtained far from the tip of the nanotube, where the catalyst particle is located, the only location in these ultralong nanotubes where multiple tubes might be expected to exist. Thus, the data shown in Figure 6 represent a true nanotube chiral shift.

**Conclusion**

These studies suggest that the CVD-grown ultralong nanotubes are of high structural quality with low defect densities and generally uniform structural characteristics across their lengths. It will be important for future efforts to correlate the observed minor structural variations with localized transport and photophysical properties to understand their potential impact on optical and electronic applications. Of particular interest in this regard is the frequency of occurrence of IMJs. If these structures are not prevalent, then the long lengths of continuous chirality available with ultralong nanotubes should display uniform device properties. If IMJs are found to be a generally occurring phenomenon, then the quick-heating CVD growth method could be an important means for rational synthesis of IMJs. More extensive probing of ultralong nanotubes will be important for obtaining better IMJ occurrence statistics. Raman imaging could provide an important means for understanding and steering growth parameters for optimized control of large-scale IMJ production and will also be important for developing a general understanding of CVD nucleation, growth, and
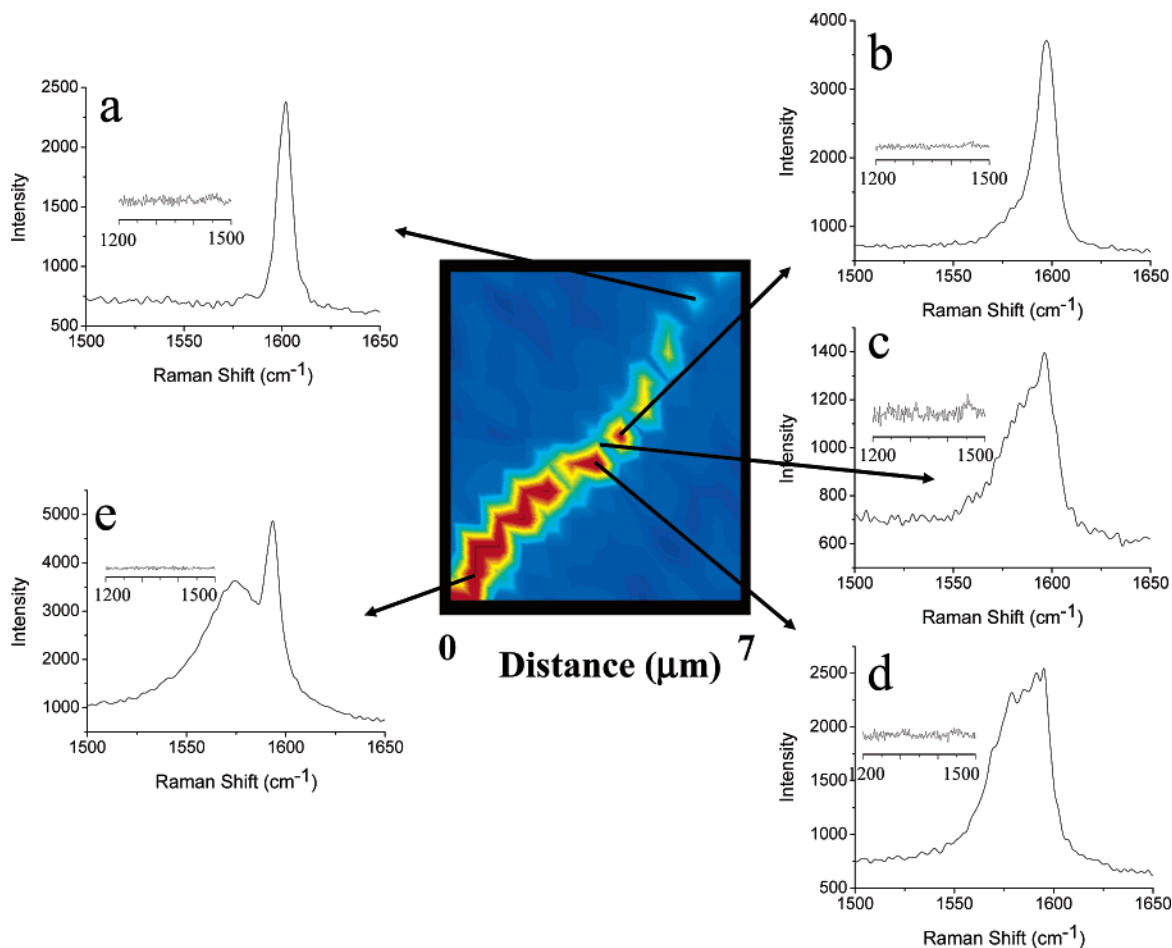
Imaging of Ultralong Carbon Nanotubes

*J. Phys. Chem. B, Vol. 109, No. 9, 2005* **3757**



**Figure 6.** Raman spectral image containing a semiconductor-to-metallic intramolecular junction (IMJ). Individual spectra along the nanotube show the (a) semiconductor region, (b–d) central transition region, and (e) metallic region. The image is taken from highlighted region d of Figure 1. The IMJ position is indicated by the black arrow in Figure 1d. Inset spectra are of the D-band region. The D-band intensity scale is the same as that for G-band spectra. The weak band at 1450 cm$^{-1}$ is a substrate peak.
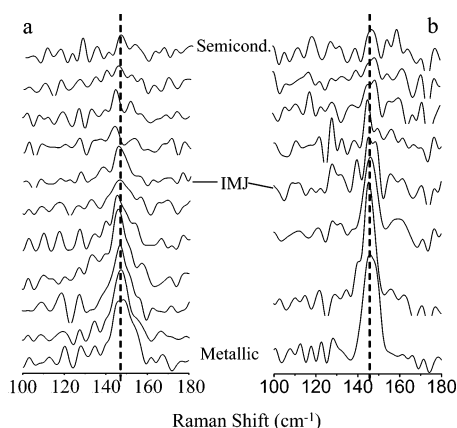


**Figure 7.** RBM spectra obtained from two images of the IMJ transition taken on separate days. Spectra in a are taken from the image shown in Figure 6. Spectra correspond (from top to bottom, respectively) to the semiconductor, through the IMJ, to the metallic region of the nanotube.

termination mechanisms through its ability to provide rapid feedback into the growth parametrization process. Thus, Raman imaging has been demonstrated to be a valuable nondestructive and complementary tool to STM and other near-field methods for structural characterization of nanotubes. This technique has the additional advantage of not being limited to probing nanotubes grown on conductive surfaces, allowing structural studies of nanotubes grown on a broad range of substrate types.

**Supporting Information Available:** Additional D- and G-band spectra of individual ultralong nanotubes and modeled Raman combination spectra and AFM data in support of the claim that only one nanotube exists in the IMJ region of Figure 6. This material is available free of charge via the Internet at http://pubs.acs.org.

**References and Notes**

(1) Huang, S.; Cai, X.; Liu, J. *J. Am. Chem. Soc.* **2003**, *125*, 5636.

(2) Huang, S.; Maynor, B.; Cai, X.; Liu, J. *Adv. Mater.* **2003**, *15*, 1651.

(3) Huang, S.; Woodson, M.; Smalley, R.; Liu, J. *Nano Lett.* **2004**, *4*, 1025.

(4) Zheng, L. X.; O'Connell, M. J.; Doorn, S. K.; Liao, X. Z.; Zhao, Y. H.; Akhadov, E. A.; Hoffbauer, M. A.; Roop, B. J.; Jia, Q. X.; Dye, R. C.; Peterson, D. E.; Huang, S. M.; Liu, J.; Zhu, Y. T. *Nat. Mater.* **2004**, *3*, 673.

(5) Jorio, A.; Saito, R.; Hafner, J. H.; Lieber, C. M.; Hunter, M.; McClure, T.; Dresselhaus, G.; Dresselhaus, M. S. *Phys. Rev. Lett.* **2001**, *86*, 1118.

(6) Dresselhaus, M. S.; Dresselhaus, G.; Jorio, A.; Souza Filho, A. G.; Saito, R. *Carbon* **2002**, *40*, 2043.

(7) Yu, Z.; Brus, L. E. *J. Phys. Chem. B* **2001**, *105*, 6831.

(8) Hartschuh, A.; Sanchez, E. J.; Xie, X. S.; Novotny, L. *Phys. Rev. Lett.* **2003**, *90*, 95503.

(9) Hayazawa, N.; Yano, T.; Watanabe, H.; Inouye, Y.; Kawata, S. *Chem. Phys. Lett.* **2003**, *376*, 174.

(10) Mews, A.; Koberling, F.; Basche, T.; Philipp, G.; Duesberg, G. S.; Roth, S.; Burghard, M. *Adv. Mater.* **2000**, *12*, 1210.

(11) Jiang, C.; Zhao, J.; Therese, H. A.; Friedrich, M.; Mews, A. *J. Phys. Chem. B* **2003**, *107*, 8742.

(12) Hadjiev, V. G.; Arepalli, S.; Jandl, S.; Yowell, L. *Nanotechnology* **2004**, *15*, 562.

(13) Li, Y.; Liu, J.; Wang, Y.; Wang, Z. L. *Chem. Mater.* **2001**, *13*, 1008.

(14) Jorio, A.; Souza Filho, A. G.; Dresselhaus, G.; Dresselhaus, M. S.; Swan, A. K.; Unlu, M. S.; Goldberg, B. B.; Pimenta, M. A.; Hafner, J. H.; Lieber, C. M.; Saito, R. *Phys. Rev. B* **2003**, *65*, 155412.

(15) Saito, R.; Gruneis, A.; Samsonidze, G. G.; Brar, V. W.; Dresselhaus, G.; Dresselhaus, M. S.; Jorio, A.; Cancado, L. G.; Fantini, C.; Pimenta, M. A.; Souza Filho, A. G. *New J. Phys.* **2003**, *5*, 157.

(16) Dillon, A. C.; Parilla, P. A.; Alleman, J. L.; Gennett, T.; Jones, K. M.; Heben, M. J. *Chem. Phys. Lett.* **2005**, *401*, 522.

(17) Cumings, J.; Mickelson, W.; Zettl, A. *Solid State Comm.* **2003**, *126*, 359.

(18) Bandow, S.; Chen, G.; Sumanasekera, G. U.; Gupta, R.; Yudasaka, M.; Iijima, S.; Eklund, P. C. *Phys. Rev. B* **2002**, *66*, 075416.

(19) Li, F.; Chou, S. G.; Ren, W.; Gardecki, J. A.; Swan, A. K.; Unlu, M. S.; Goldberg, B. B.; Cheng, H.-M.; Dresselhaus, M. S. *J. Mater. Res.* **2003**, *18*, 1251.

(20) Freitag, M.; Chen, J.; Tersoff, J.; Tsang, J. C.; Fu, Q.; Liu, J.; Avouris, P. *Phys. Rev. Lett.* **2004**, *93*, 076803.

(21) Li, Y. M.; Kim, W.; Zhang, Y. G.; Rolandi, M.; Wang, D. W.; Dai, H. J. *J. Phys. Chem. B* **2001**, *105*, 11424.

(22) Jorio, A.; Dresselhaus, G.; Dresselhaus, M. S.; Souza, M.; Dantas, M. S. S.; Pimenta, M. A.; Rao, A. M.; Saito, R.; Liu, C.; Cheng, H. M. *Phys. Rev. Lett.* **2000**, *85*, 2617.

(23) Brown, S. D. M.; Jorio, A.; Corio, P.; Dresselhaus, M. S.; Dresselhaus, G.; Saito, R.; Kneipp, K. *Phys. Rev. B* **2001**, *63*, 155414.

(24) Pimenta, M. A.; Marucci, A.; Empedocles, S. A.; Bawendi, M. G.; Hanlon, E. B.; Rao, A. M.; Eklund, P. C.; Smalley, R. E.; Dresselhaus, G.; Dresselhaus, M. S. *Phys. Rev. B* **1998**, *58*, R16016.

(25) Kataura, H.; Kumazawa, Y.; Maniwa, Y.; Umezu, I.; Suzuki, S.; Ohtsuka, Y.; Achiba, Y. *Synth. Met.* **1999**, *103*, 2555.

(26) Rao, A. M.; Eklund, P. C.; Bandow, S.; Thess, A.; Smalley, R. E. *Nature* **1997**, *388*, 257.

(27) Sumanasekera, G. U.; Allen, J. L.; Fang, S. L.; Loper, A. L.; Rao, A. M.; Eklund, P. C. *J. Phys. Chem. B* **1999**, *103*, 4292.

(28) Kavan, L.; Rapta, P.; Dunsch, L.; Bronikowski, M. J.; Willis, P.; Smalley, R. E. *J. Phys. Chem. B* **2001**, *105*, 10764.

(29) Strano, M. S.; Huffman, C. B.; Moore, V. C.; O'Connell, M. J.; Haroz, E. H.; Hubbard, J.; Miller, M.; Rialon, K.; Kittrell, C.; Ramesh, S.; Hauge, R. H.; Smalley, R. E. *J. Phys. Chem. B* **2003**, *107*, 6979.

(30) Hadjiev, V. G.; Iliev, M. N.; Arepalli, S.; Nikolaev, P.; Files, B. S. *Appl. Phys. Lett.* **2001**, *78*, 3193.

(31) McEuen, P. L. *Nature* **1998**, *393*, 15.

(32) Yao, Z.; Postma, H. W. Ch.; Balents, L.; Dekker, C. *Nature* **1999**, *402*, 273.

(33) Baughman, R. H.; Zakhidov, A. A.; de Heer, W. A. *Science* **2002**, *297*, 787.

(34) Lambin, Ph.; Fonseca, A.; Vigneron, J. P.; Nagy, J. B.; Lucas, A. A. *Chem. Phys. Lett.* **1995**, *245*, 85.

(35) Charlier, J.-C.; Ebbesen, T. W.; Lambin, Ph. *Phys. Rev. B* **1996**, *53*, 11108.

(36) Chico, L.; Crespi, V. H.; Benedict, L. X.; Louie, S. G.; Cohen, M. L. *Phys. Rev. Lett.* **1996**, *76*, 917.

(37) Saito, R.; Dresselhaus, G.; Dresselhaus, M. S. *Phys. Rev. B* **1996**, *53*, 2044.

(38) Ferreira, M. S.; Dargam, T. G.; Muniz, R. B.; Latge, A. *Phys. Rev. B* **2000**, *62*, 16040.

(39) Fa, W.; Yang, X.; Chen, J.; Dong, J. *Phys. Lett. A* **2004**, *323*, 122.

(40) Ouyang, M.; Hunag, J.-L.; Cheung, C. L.; Lieber, C. M. *Science* **2001**, *291*, 97.

(41) Kim, H.; Lee, J.; Kahng, S.-J.; Son, Y.-W.; Lee, S. B.; Lee, C.-K.; Ihm, J.; Kuk, Y. *Phys. Rev. Lett.* **2003**, *90*, 216107.